Biophysical Journal
Article

Biophysical Society

Principles and practice for SARS-CoV-2 decontamination of N95 masks with UV-C

Thomas Huber,[1,*] Olivia Goldman,[2] Alexander E. Epstein,[3] Gianna Stella,[4] and Thomas P. Sakmar[1,*]
[1]Laboratory of Chemical Biology and Signal Transduction, Tri-Institutional Program in Chemical Biology, , [2]Laboratory of Neurogenetics and Behavior, , [3]David Rockefeller Graduate Program, , and [4]Tri-Institutional Program in Chemical Biology, The Rockefeller University, New York, New York

ABSTRACT A mainstay of personal protective equipment during the coronavirus disease 2019 pandemic is the N95 filtering facepiece respirator. N95 respirators are commonly used to protect healthcare workers from respiratory pathogens, including the novel coronavirus severe acute respiratory syndrome coronavirus 2, and are increasingly employed by other frontline workers and the general public. Under routine circumstances, these masks are disposable, single-use items, but extended use and reuse practices have been broadly enacted to alleviate critical supply shortages during the coronavirus disease 2019 pandemic. Although extended-time single use presents a low risk of pathogen transfer, repeated donning and doffing of potentially contaminated masks presents increased risk of pathogen transfer. Therefore, efficient and safe decontamination methods for N95 masks are needed to reduce the risk of reuse and mitigate local supply shortages. Here, we review the available literature concerning use of germicidal ultraviolet-C (UV-C) light to decontaminate N95 masks. We propose a practical method for repeated point-of-use decontamination using commercially available UV-C cross-linker boxes from molecular biology laboratories to expose each side of the mask to 800–1200 mJ/cm^2 of UV-C. We measure the dose that penetrated to the interior of the respirators and model the potential germicidal action on coronaviruses. Our experimental results, in combination with modeled data, suggest that such a UV-C treatment cycle should induce a >3-log-order reduction in viral bioburden on the surface of the respirators and a 2-log-order reduction throughout the interior. We find that a dose 50-fold greater does not impair filtration or fit of 3M 8210 N95 masks, indicating that decontamination can be performed repeatedly. As such, UV-C germicidal irradiation is a practical strategy for small-scale point-of-use decontamination of N95s.

SIGNIFICANCE The coronavirus disease 2019 pandemic has uncovered critical supply shortages of N95 masks, which are key personal protective equipment for healthcare and other essential workers. Here, we investigate the short-wavelength ultraviolet-C light penetration into the interior of the porous filtration layers of a standard N95 mask. Our experiments and critical review of the literature allow us to conclude that ultraviolet-C decontamination of N95 masks is feasible and should be superior to chemical decontamination strategies that risk damaging the delicate surface electrostatics of the active filtering material.

INTRODUCTION

The recent severe acute respiratory syndrome coronavirus 2 (SARS-CoV-2) outbreak has created a worldwide shortage of personal protective equipment (PPE), which leaves healthcare workers dangerously ill-equipped to aid coronavirus disease 2019 (COVID-19) patients (1). Respiratory viruses such as SARS-CoV-2 can potentially be transmitted through contact, respiratory droplets, and aerosols. The World Health Organization recommends droplet and contact precautions for people caring for COVID-19 patients and recommends airborne precautions, such as N95 masks, for circumstances where SARS-CoV-2 aerosol particles are generated (2).

N95 masks are filtering facepiece respirators that have at least 95% efficiency for filtering airborne particles (size around 300 nm) and meet the air filtration rating of the US National Institute for Occupational Safety and Health classification for filtering respirators. Equivalent standards of N95 are FFP2 (European Union), KN95 (China), DS/DL2 (Japan), and KF94 (South Korea) (3). N95 filtering facepiece respirators for use by the general public in public health medical emergencies are intended for over-the-counter use (4). A

Submitted August 31, 2020, and accepted for publication February 23, 2021.

*Correspondence: ; hubert@rockefeller.edu or sakmar@rockefeller.edu

Editor: Tamar Schlick.
https://doi.org/10.1016/j.bpj.2021.02.039

model for a hypothetical influenza pandemic in the US suggested that several billion N95 masks would be required to prevent widespread transmission among the public, which would lead to severe supply shortages (5). Current guidelines during the COVID-19 pandemic suggest limiting the use of N95 masks to healthcare personnel while providing low-tech face masks for the general public (6).

Typically, N95 masks are discarded after each use to prevent exposure of infectious material on the respirator to others or the wearer, and extended single use is recommended rather than reuse in the case of pathogens for which contact transmission is possible (7,8). However, because of shortages of PPE, many healthcare workers are not only wearing N95 masks for extended periods of time but also reusing them (9).

There are challenges in maintaining the physical and electrostatic properties of N95 masks after certain decontamination methods. The multilayer sandwich structure of N95 masks, like the 3M model 8210 (Fig. 1), consists of an outer layer (coverweb) that faces the environment, middle layers (filters 1 and 2), and an inner layer (shell) that faces the user (10). The 3M 8210 mask materials are polyester for the coverweb and shell, polypropylene for filters 1 and 2, thermoplastic elastomer for the straps, aluminum for the nose clip, and polyurethane for the nose foam. Filters 1 and 2 are the internal filtering medium, the key material of the N95 mask. The internal filtering medium is a proprietary Brownian filtration media that traps particles that collide with a specially treated surface, which is made of electrostatically charged meltblown polypropylene microfibers. These microfibers have cross-sectional diameters in the range of 2–10 μm and cross each other to form a three-dimensional porous structure with up to 90% porosity (3). The microfibers are electrostatically charged to attract and trap particles and increase filtration efficiency without impeding air flow (11). Decontamination methods with 75% alcohol or a chlorine-based solution dramatically reduce the filtration performance of N95 masks, likely because of breakdown of the electrostatic charge on the filter material, and are not recommended (3). On the other hand, ultraviolet germicidal irradiation (UVGI) has been shown to efficiently inactivate pandemic influenza virus applied as aerosols or droplets on several different N95 masks (12–14).

Recent work has optimized or implemented UVGI (15), vaporized hydrogen peroxide (16), and moist heat (17) for large-scale decontamination of N95s in hospitals. However, there is a need for inexpensive, widely available tools for small-scale mask decontamination. We demonstrate that UV germicidal irradiation represents a powerful tool for small-scale decontamination of N95 masks. To justify a minimal irradiation dosage for safe decontamination, we model the germicidal action of UV irradiation in the filter material of the N95 mask. We show that N95 decontamination can be achieved with commercially available UV cross-linker devices commonly found in molecular biology laboratories. Similar low-cost UV boxes designed for point-of-use N95 mask decontamination could be rapidly produced and distributed worldwide to alleviate local critical shortages of N95 masks, such as during the ongoing COVID-19 pandemic.

MATERIALS AND METHODS

UV-C transmittance measurements

The hemispherical transmittance of a scattering medium is usually measured with an integrating sphere. A simple alternative is to use an optical diffusor, such as an opal glass or filter paper behind the sample (18).

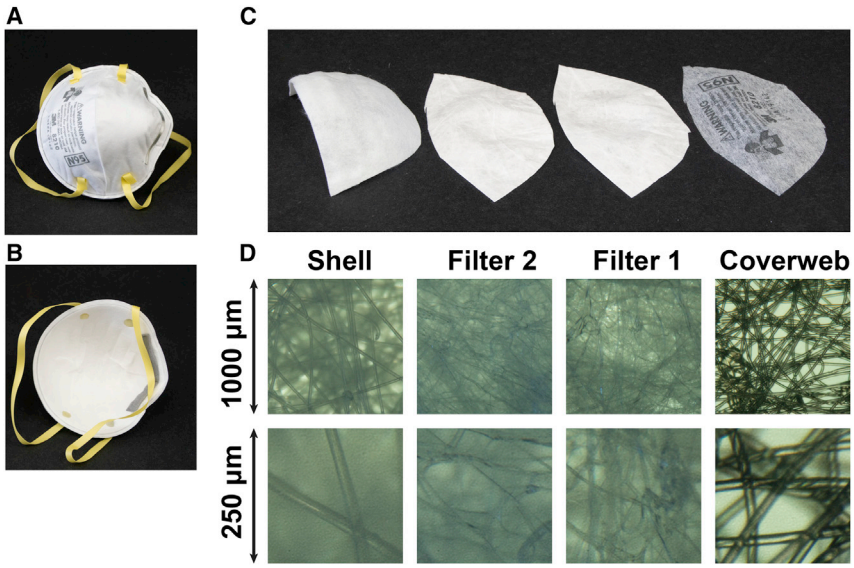

FIGURE 1 The multilayer sandwich anatomy of the N95 mask using the 3M Company 8210 mask as an example. (*A*) Environmental interface. (*B*) User interface. (*C*) From left to right: inner layer (shell), middle layers (filter 2 and filter 1), and outer layer (coverweb). (*D*) Light microscope images of the four layers, with lower row at fourfold higher magnification. To see this figure in color, go online.

The hemispherical transmittance (T) can be calculated from the ratio of the transmitted irradiance (E_e^t) and the incident irradiance (E_e^i):

$$T = \frac{E_e^t}{E_e^i}. \quad (1)$$

Transmittance measurement with UV-visible light spectroscopy

To determine the absorbance spectrum of each of the different layers of the N95 mask, we adapted a method normally used for scattering suspensions (18). We placed a piece of Whatman filter paper as a light diffuser behind the blank and sample cuvette holder in a double-beam UV-visible light spectrophotometer (Lambda 800; Perkin Elmer, Waltham, MA). We taped a piece of the mask material in front of the filter paper (thickness 0.34 mm; Whatman 3030–917 cellulose chromatography paper 3MM; Sigma-Aldrich, St. Louis, MO) in the sample position. In this way, the light diffuser collected a representative sample of the scattered light penetrating the mask material. We recorded spectra with a slit width corresponding to a 2-nm bandpass with an integration time of 0.4 s for each data point sampled in 1-nm intervals between 700 and 250 nm.

Transmittance measurement with UV-C radiometry

We used a high-intensity 254-nm UV light source (UVP CL-1000; Analytik Jena US, Upland, CA) and a UV-C light meter (UV254SD; General Tools, Secaucus, NJ) to measure the irradiance with and without a piece of each different layer of the N95 mask in front of the sensor. We calculate the transmittances using Eq. 1.

We also used a 254-nm UVP Compact UV lamp that facilitates measuring the transmittance of the materials without the need to turn off the lamp when changing the samples. The transmittances were 22% (16–29), 21% (16–26), 14% (9–20), and 0% (0–5) for the coverweb, filter 1, filter 2, and shell, respectively. Values in parentheses are 95% confidence intervals (95% CIs) from nine repeated sets of measurements, including the dominant contribution from the specified measurement accuracy of the UV254SD meter, which is ± 0.082 mW/cm^2. The lower power of the UVP Compact UV lamp as compared with the UVP CL-1000 source did not allow a nonzero measurement for the optically dense material of the shell layer. Therefore, we used a densitometric method to quantify more accurately the transmittance of the shell layer.

Densitometric UV radiometry

We used photochromic intensity indicators (New UV Intensity Labels, UV Process Supply, Chicago, IL) for direct UV densitometry measurements (Fig. 2). These yellow-colored labels change gradually to green when exposed to UV. We determined the UV dose-dependent change in color by exposing a set of labels to increasing UV dosages in the UVP CL-1000 source. We simultaneously recorded the UV irradiance with the UV254SD meter using a 1-s sampling interval to obtain the actual exposure dosage by numerical integration. We quantified the color change using a flatbed scanner (Epson, Los Alamitos, CA) and Fiji or ImageJ for image analysis. The red channel of the RGB image showed the largest change of photochromic effect. Exponential fitting of the dose-dependent data with Prism (Graphpad) showed that a dose of 88 mJ/cm^2 (95% CI 77–103) yields a half-maximum photochromic effect.

We exposed labels sequentially through the shell layer material for 60 min in the UVP CL-1000 source. We quantified the color changes of these labels under identical conditions to the labels for the calibration.

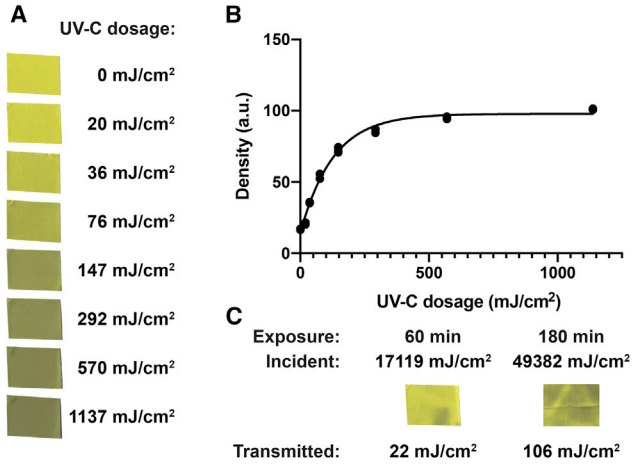

FIGURE 2 Densitometric UV-C radiometry and transmittance of shell material. (*A*) Color change of UV intensity label stamps upon exposure with increasing UV-C dosage. (*B*) Exponential fit of the density of the stamps quantified as the mean inverted red channel intensity of the flatbed scanner image. (*C*) UV intensity labels exposed through the shell material of the 3M 8210 N95 mask for 60- and 180-min exposures in the UVP CL-1000 cross-linker. The incident exposure was quantified by integration of the UV-C meter reading sampled in 1-s intervals. The transmitted exposure is quantified using the calibration curve from (*B*). To see this figure in color, go online.

The 60-min exposure with an integrated UV surface dosage of 17,119 mJ/cm^2 resulted in a color change that corresponds to a transmitted dosage of 22 mJ/cm^2 (95% CI 17–26). The ratio of the transmitted/surface dosages gives the total transmission, which is 0.13% (95% CI 0.10–0.15). We noticed that the color change across the label was uneven, for example, with less change beneath a wrinkle in the shell layer, because of the manufacturing of the dome-shaped structure.

Next, we exposed an array of intensity labels to map the intensity distribution of the transmitted light. We used a 180-min exposure with 49,382 mJ/cm^2 surface dosage to map the transmitted light intensity distribution in a 5-cm^2 region under the shell layer material. The average color change corresponds to a transmitted dosage 106 mJ/cm^2 (95% CI 97–116), which gives 0.21% (95% CI 0.20–0.23). The one-standard-deviation-wide range of color changes corresponds to a range of transmitted dosages from 0.13 to 0.34%. The 95% range of color changes observed for the transmitted light corresponds to a range of transmitted dosages from 0.07 to 5.7%.

Modeling the UV-C light distribution in the multilayer structure of the N95 mask

The transmittance of the i-th layer (T_i) is related to its thickness (d_i) by an attenuation coefficient (α_i):

$$T_i = \exp(-\alpha_i d_i). \quad (2)$$

We define a depth-dependent attenuation coefficient as a step function corresponding to the attenuation coefficients of all n layers:

$$\alpha(z) = \begin{cases} \alpha_i, \sum_{j=1}^{i-1} d_j < z \le \sum_{j=1}^{i} d_j \text{ for } i = 1 \text{ to } n \\ 0, \text{ otherwise} \end{cases}. \quad (3)$$

Integration of the depth-dependent attenuation coefficient yields the optical thickness (τ) at depth (d):

$$\tau(d) = \int_0^d \alpha(z)dz\,. \tag{4}$$

The depth-dependent transmittance ($T(d)$) is related to the optical thickness by

$$T(d) = \exp(-\tau(d))\,. \tag{5}$$

The model neglects the contributions of multiple reflections between the layers of materials, which is small because of the poor reflectance of materials in the short-wavelength UV-C region. We confirmed the validity of our model by control experiments measuring the transmittance of stacks of identical layers of material that give a linear increase of total optical thickness with the number of layers.

The optical thickness in the reverse direction (τ_R) is obtained by integration of the interval starting at the depth (d) and ending at the combined thickness of all layers ($\sum d_i$):

$$\tau_R(d) = \int_d^{\sum d_i} \alpha(z)dz\,. \tag{6}$$

Here, we define the depth-dependent transmittance in reverse direction ($T_R(d)$) as

$$T_R(d) = \exp(-\tau_R(d)). \tag{7}$$

The exposure dosage (D) is related to the exposure time (t) and the irradiance (E_e):

$$D = E_e t\,. \tag{8}$$

The depth-dependent exposure dosage ($D(d)$) is given by the surface exposure in the forward direction (D), the surface exposure in the reverse direction (D_R), and the depth-dependent transmittances:

$$D(d) = DT(d) + D_R T_R(d). \tag{9}$$

Modeling the virus viability in the N95 mask

We define the survival (s) as the ratio of the number of infectious virions after exposure (n) and before exposure (n_0):

$$s = n / n_0. \tag{10}$$

The simplest dose-dependent survival function ($s(D)$) for single-hit kinetics of UV inactivation of virus infectivity relates the exposure dosage ((D)) to a UV rate constant (k):

$$s(D) = \exp(-kD). \tag{11}$$

We also use a second model with a secondary population of viruses with a different rate constant (k') that comprises a fraction (f) of the total population:

$$s(D) = (1-f)\exp(-kD) + f\exp(-k'D). \tag{12}$$

The average survival (s) can be calculated from a depth-dependent density of viruses before exposure ($\sigma_0(d)$), the survival function, and the depth-dependent exposure dosage:

$$s = \int_0^{\sum d_i} \sigma_0(z)s(D(z))dz \Big/ \int_0^{\sum d_i} \sigma_0(z)dz. \tag{13}$$

The figures are modeled with a constant value for $\sigma_0(d)$ corresponding to uniform contamination of the mask layers. We also use a unit value for the thickness for each layer (d_i). Together, these two choices give each layer the same share to the overall virus survival. A more advanced model would include a nonlinear distribution of virus load trapped across the different layers of the mask, based on the adsorption kinetics of the viral particles on the internal surface area of the various layers of different microfiber materials.

RESULTS

Physical dimensions

We determined the thickness and areal density for each of the materials of the four layers of the 3M 8210 N95 mask (see Fig. 1). The coverweb, filter 1, filter 2, and shell layers are 0.20, 0.36, 0.41, and 0.90 mm thick, respectively, and have areal densities of 4.2, 5.1, 5.5, and 16.4 mg/cm^2. The thickness and areal density measurements have relative errors of ± 20 and ± 15%, respectively. Note that the thickness of these highly compressible materials is very difficult to measure, and we obtained our best estimated of the thickness by limiting the manually applied measurement force on a standard Vernier caliper (Mitutoyo, Kawasaki, Japan). Light microscopy revealed that the fibers within each layer are 16 μm (95% CI, 12–20) thick in the coverweb, 5.5 μm (95% CI, 3.9–7.1) thick in filter 1, 2.8 μm (95% CI, 0.7–4.8) thick in filter 2, and 21 μm (95% CI, 19–24) thick in the shell. The packing volume fraction of the microfibers can be approximated as $\sigma/\rho d_0$, where σ is the areal density, ρ is the density of the bulk polymer, and d_0 is the layer thickness. With a density for neat polyester of 1.68 g/cm^3 (for polyethylene terephthalate) and for neat polypropylene of 0.9 g/cm^3, we estimate the packing volumes fractions as 11, 15, 16, and 13% for the shell, filter 2, filter 1, and coverweb, respectively. The relative internal surface area of the microfibers compared to the macroscopic area of the filter layer can be approximated as $4\sigma/\rho d$, where σ is the areal density, ρ is the density, and d is the fiber thickness. We estimate the relative internal surface areas as 19 for the shell, 87 for filter 2, 41 for Filter 1, and 6 for the coverweb.

Penetration of UV-C light into N95 mask layers

A central question is how much germicidal UV light penetrates the different layers of an N95 mask. The optical transmittance of the mask layers is hard to quantify for short-wavelength UV-C light, especially for the optically dense

shell layer of the N95 mask studied here. We used three complementary methods—spectrophotometry, radiometry, and densitometry—to determine that the optical transmittance of the shell layer is only 0.1% of the incident irradiance.

Fig. 3 shows the spectrophotometric optical transmittance of the different layers of the 3M 8210 N95 mask. The transmittance of the two middle layers (filter 1 and filter 2) in the UV-C range is higher than that of the inner layer (shell). The shell transmits little UV-C light because it is made from polyester, which is an aromatic polymer that absorbs UV. By contrast, filters 1 and 2 are made of polypropylene, which has low specific UV absorption besides losses due to light scattering. The coverweb, despite being made out of UV-absorbing polyester, is the thinnest of all layers and shows transmittance that is similar to that of the filter layers.

Because the stray light performance of the spectrophotometer limits the accuracy of the measurements by systematically overestimating transmittance, we employed UV-C radiometry as an alternative approach to measure the spectral transmission of N95 mask materials (setup 2 in Fig. 3 *D*). The transmittances are 15, 27, 21, and 0.11% for the coverweb, filter 1, filter 2, and shell, respectively. The limitation of setup 2 is that the sample and the digital radiometer have to be placed into the UVP CL-1000 photo-crosslinker before the UV light can be turned on, which makes it difficult to measure fluctuations of the intensity. In setup 3, we used the UVP Compact UV lamp, enabling us to perform repeated measurements with and without samples to determine the transmittance based on the radiometer readings. The calculated transmittances were 22% (16–29), 21% (16–26), 14% (9–20), and 0% (0–5) for the coverweb, filter 1, filter 2, and shell, respectively. Because the irradiance of the Compact UV lamp was lower as compared to the CL-1000, the transmitted light was too low to give any readings different from zero on the radiometer. To determine the transmittance of the shell layer material, we resorted to a densitometric approach using photochromic UV-C indicator stickers. With two different exposure times (60 min for setup 4 and 180 min for setup 5), we could measure the transmission of the shell layer as 0.13% (95% CI 0.10–0.15) for setup 4 and 0.21% (95% CI 0.20–0.23) for setup 5. Our preferred transmittance values as indicated in Fig. 3 *E* are from setup 3 for the layers coverweb, filter 1, and filter 2 and from setup 5 for the shell layer.

Germicidal UV sources

The 254-nm line of the mercury-vapor emission spectrum is the predominant line of a low-pressure mercury-vapor lamp manufactured with a soda-lime glass bulb, which absorbs the 184-nm line. The 254-nm UV-C light efficiently inactivates single-stranded RNA viruses as seen in the germicidal action spectrum (Fig. 3 *C*; (19)). The action spectrum is for the MS2 bacteriophage, which is a positive-strand RNA virus similar to the coronaviruses of interest. The shape of the germicidal action spectrum should be independent of the particular virus but instead should depend on the underlying photochemistry of the UV damage of the RNA genome. Recently, germicidal UV light-emitting diodes became commercially available that emit in the 260–280 nm range.

UV-C light sensitivity of SARS-CoV

The sensitivity of RNA viruses depends on several factors, such as genome size and base composition (20). Moreover, the UV-C dose-dependent inactivation of viruses is known to deviate from a simple first-order decay model (21). In the absence of detailed data on the novel coronavirus SARS-CoV-2, we use literature data for the closely related virus SARS-CoV (22), as the UV-C sensitivity of related viruses is roughly constant after accounting for genome size (23).

Fig. 4 shows a semilogarithmic plot of the dose-dependent inactivation of SARS-CoV measured by Kariwa et al. (22,24). The endpoint dilution assay quantifies the virus titer by serially diluting the treated virus stock, inoculating Vero E6 cells with the serial dilutions, observing the cytopathic effect under a microscope after 48 h incubation to quantify the percentage of cell death, and calculating the 50% tissue culture infective dose. We model the data as a double-exponential decay function that enables interpolation of the data points in a meaningful manner. The fast component is 98.6 $\pm$ 0.4% and has a UV-C sensitivity of 0.522 $\pm$ 0.040 cm^2/mJ. The slow component is 1.4 $\pm$ 0.4% and has a sensitivity of 0.066 $\pm$ 0.003 cm^2/mJ. The occurrence of a slow component of UV-resistant virus is unexpected. Exponential survival curves can be explained by a single hit to kill model (25). Lytle and Sagripanti compare the UV-C sensitivities of a large number of different virus families and state that only the Herpesviridae family consistently exhibits two-component survival curves (23). Therefore, it is likely that the double-exponential decay function necessary to fit the Kariwa et al. data reflects an experimental issue. We interpret the slow component as virus trapped at the bottom of the sample and the fast component as freely diffusing virus particles. If so, the fast rate constant would represent the averaged depth-dependent UV-C dosage scaled by the sensitivity of the virus. The slow component would result from the attenuated UV-C dosage reaching the bottom, caused by the inner-filter effects of the tissue culture media used in the experiments (see the Discussion). The final plateau with a value of 17 $\pm$ 2 $TCID_{50}$/mL, which corresponds to a fraction of 5×10^{-7}, corresponds to the detection limit of the assay, which is likely due to cytopathic effects of protein components of the virions that are not inactivated by the UV-C irradiation because the assay in principle does not discriminate cytopathic effects from true infectivity like other assays.

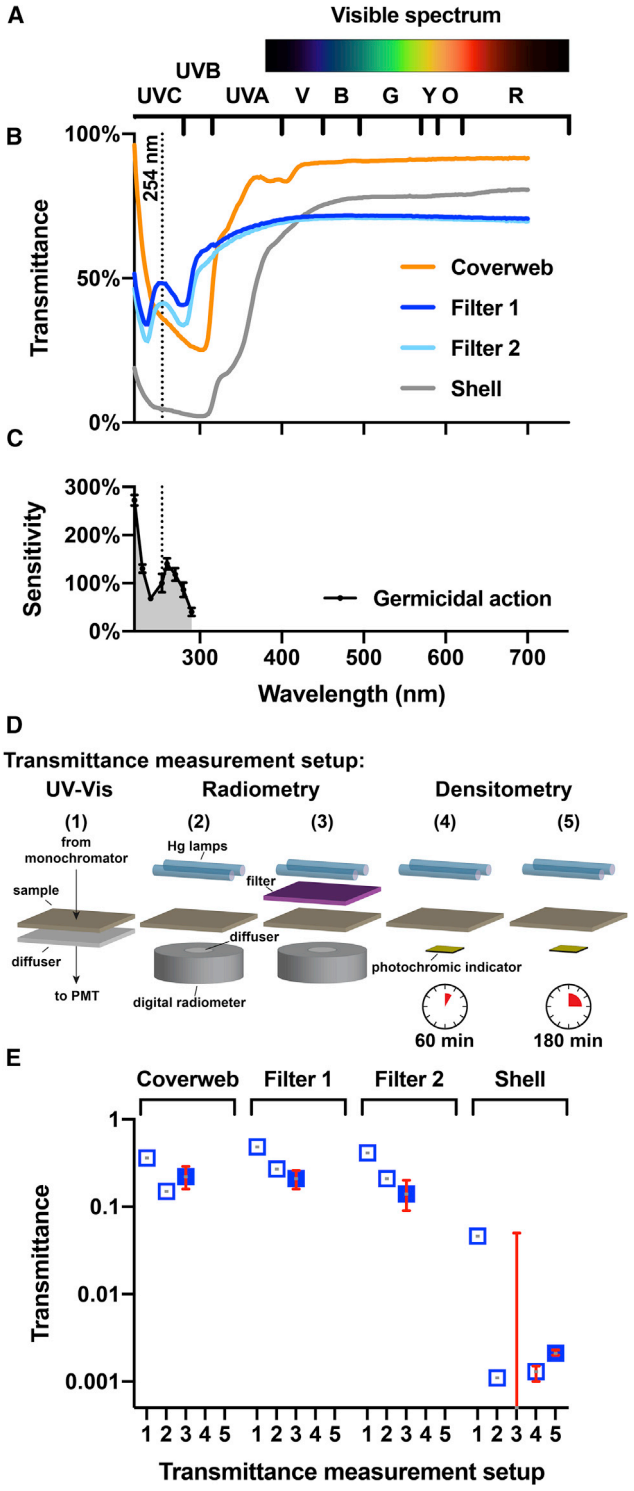

FIGURE 3 Optical transmittance of N95 mask materials and spectral sensitivity of viral RNA. (*A*) Colors of the visible spectrum. Wavelength ranges corresponding to different colors (R, red; O, orange; Y, yellow; G, green; B, blue; V, violet) and ultraviolet A, B, and C (UV-A, UV-B, UV-C) are shown. (*B*) Optical transmittance of the four layers of the 3M 8210 N95 mask (coverweb, filter 1, filter 2, and shell). The dotted line indicates the location of the strong 254-nm line of the spectrum of a low-pressure mercury-vapor lamp. (*C*) Germicidal action spectrum shows the wavelength-specific sensitivity of single-stranded RNA viruses. The sensitivity is calculated as the inactivation rate constants for viral infectivity normalized to the value at 254 nm, as determined for the MS2 bacteriophage (19). (*D*) Illustration of the five different experimental setups for transmittance measurement. Sample refers to the different mask materials. (*E*) Transmittance estimates for the four layers of the 3M 8210 mask using the five setups. The solid symbols correspond to our preferred transmittance values used in the models. Error bars correspond to the 95% CIs. To see this figure in color, go online.

Modeling the UV-C light distribution in the N95 mask

The relationship of the total optical transmittance and thickness for a scattering and absorbing media should follow an exponential relationship, in which an attenuation coefficient replaces the absorption coefficient of the Beer-Lambert law for nonscattering media. It is based on integrating the time-dependent photon diffusion equation often used to model light penetration into scattering media (26). To calculate the attenuation coefficient from the total transmission, we need the actual thickness of each layer.

We use the radiometric UV-C transmittance data to model the depth-dependent UV-C dosage in an N95 mask. From the preferred transmittance values (Fig. 3 *E*), we calculate that the absorbances of the four layers calculated from the transmittance data are 2.68, 0.85, 0.68, and 0.66 for the shell, filter 2, filter 1, and coverweb, respectively. We model the depth-dependent cumulative absorbance of all layers as a piecewise linear function corresponding to the sum of the absorbances, with one function from each side. These depth-dependent absorbance functions allow calculation of the depth-dependent transmittance and therefore the local UV-C dosage.

Fig. 5 *A* shows a semilogarithmic plot with three curves corresponding to the local UV-C dosage as a function of the relative position in the four layers of the N95 mask (shell, filter 2, filter 1, and coverweb) for three cases of illumination. The first case is illumination from the inside surface of the mask. The orange curve shows the local dosage for illumination from the user-facing inside of the mask with a surface UV-C dosage of 1000 mJ/cm^2. Because of the high absorbance of the polyester material of the shell layer, the local dosage rapidly drops to 2 mJ/cm^2 at the interface between the layers shell and filter 2. It further drops to 0.29 mJ/cm^2 at the interface between filter 2 and filter 1 and to 0.06 mJ/cm^2 at the interface between filter 1 and coverweb. The residual local dosage at the exit on the other side of the mask is only 0.014 mJ/cm^2. The second case is illumination from the outside surface of the mask. The green curve shows the local dosage for illumination from the environment-facing outside of the mask with a surface UV-C dosage of 1000 mJ/cm^2. The dosage drops to 220 mJ/cm^2 at the interface between the coverweb and filter 1, to 46 mJ/cm^2 at the interface between filter 1 and filter 2, and to 6.5 mJ/cm^2 at the interface between filter 2 and the shell. The exit dosage at the inside surface is 0.014 mJ/cm^2. The third case is for

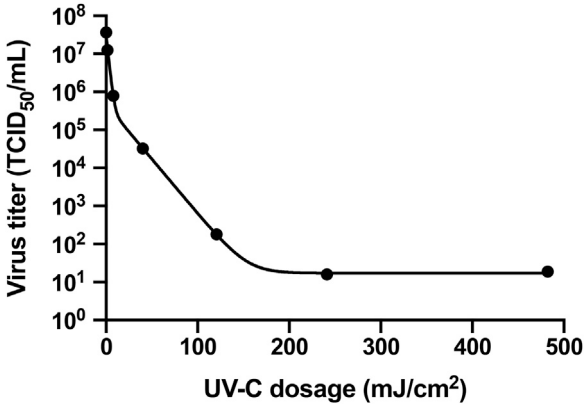

FIGURE 4 UV-C dose-dependent inactivation of SARS-CoV. We fitted the original experimental data in Kariwa et al. (22,24) to a double exponential model.

illumination from both sides of the mask. The black curve shows the local dosage for illumination from both sides of the mask with a surface UV-C dosage of 1000 mJ/cm^2 each. The local dosage is 8.6 mJ/cm^2 at the shell to filter 2 interface, 46 mJ/cm^2 at the filter 2 to filter 1 interface, and 220 mJ/cm^2 at the filter 1 to coverweb interface. The minimum of the black curve is in the core of the shell material, close to the filter 2 layer, where the local dosage is 7.4 mJ/cm^2. Therefore, the core of the N95 mask receives 270-fold less UV-C light as compared to total surface exposure of 2000 mJ/cm^2. Notably, a previous attempt to estimate the reduction of UV-C light in the interior of the 3M 8210 mask concluded that there was only a 16.4-fold reduction of UV-C dosage (27), which we conclude is based on an incorrect mathematical treatment of the radiometric observables.

Modeling the virus viability in the N95 mask

The local UV-C dosage calculated for the three cases of illumination together with the UV-C dose-dependent inactivation of SARS-CoV enables an estimate of the local residual virus viability in an irradiated N95 mask (Fig. 5 *B*). The orange curve is for the first case with illumination from the inside surface of the mask. The first half of the shell layer is efficiently decontaminated, with 0.07% local viability in the center of the shell. However, the sharp rise of the local viability to 34% at the interface of the shell and filter 2 shows that the illumination from the inside of the mask is insufficient to decontaminate the highly porous material of the shell layer. Note that the optically dense shell layer has a thickness of 0.90 mm, which is almost as much as the combined thickness of all other layers (filter 2 is 0.41 mm, filter 1 is 0.36 mm, and the coverweb is 0.20 mm thick). In contrast, the green curve for the second case, in which the mask is illuminated from the outside, shows efficient decontamination of the three layers coverweb, filter 1, and filter 2, with 4.3% local viability at the

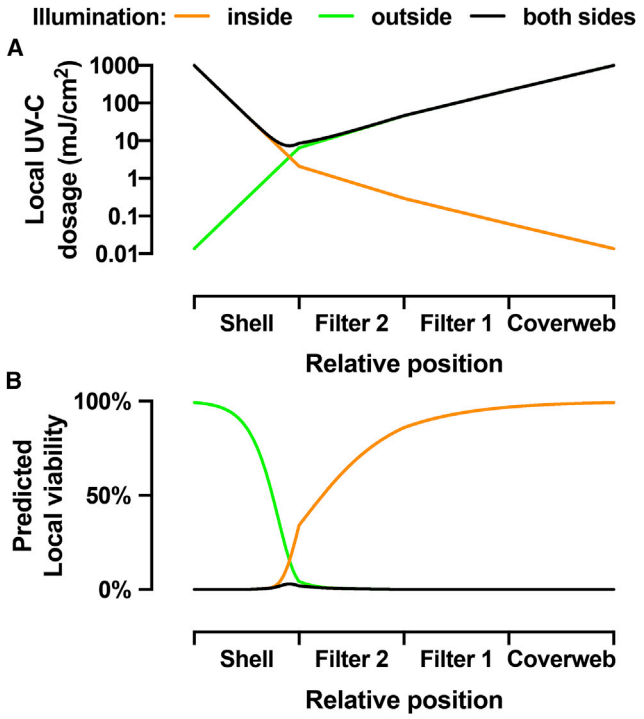

FIGURE 5 Modeling of the UV-C dosage and virus viability in different layers of the N95 mask. (*A*) Local UV-C dosage as a function of the relative position inside the four layers of the N95 mask. The three different curves show the local UV dosage for three cases of illumination: illumination from the inside only (*orange*), illumination from the outside only (*green*), and illumination from both sides (*black*) with 1000 mJ/cm^2 surface UV-C dosage. (*B*) Predicted local virus viability calculated from the local UV-C dosage distributions for the three cases. To see this figure in color, go online.

interface of filter 2 and shell, but little or no decontamination of the shell. For the third case with illumination from both sides, the local viability throughout the mask is very low. The smallest UV-C dosage inside the core of the shell material results in 3% local virus viability. The integrated local viability yields the averaged virus viability in the mask, which is 0.3% for illumination from each side together of the mask with 1000 mJ/cm^2 surface dosage.

Modeling the UV-C dose-dependent virus inactivation

Here, we analyze the dose-dependent decontamination levels and the effect of different models of UV-C sensitivity on the achievable degree of decontamination. As explained in the Discussion, previous literature disagrees on different UV-C sensitivity of coronaviruses and other related viruses (22,24,28–30). Therefore, out of an abundance of caution, we determined the proper UV-C dosage to sufficiently decontaminate N95 masks based on three different models of virus viability as a function of UV-C dose (Fig. 6 *B*). We also estimated local viability as a function of mask position assuming a standard 1000 mJ/cm^2 exposure (Fig. 6 *A*).

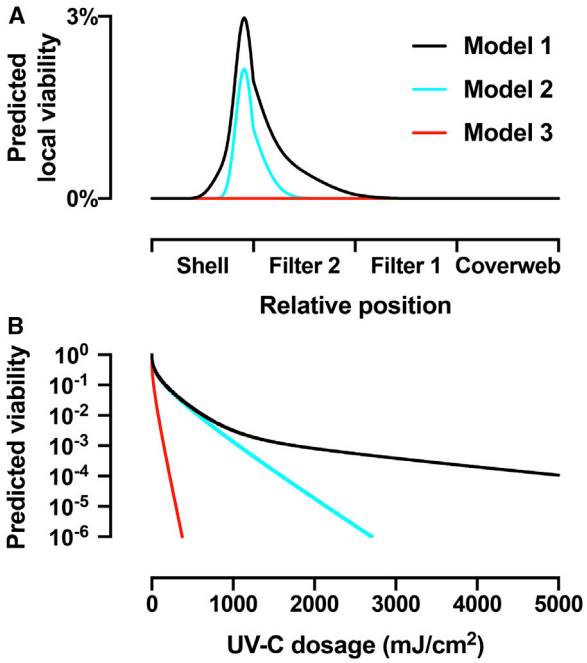

FIGURE 6 Modeling of the virus viability for three different models of UV-C sensitivity. (*A*) Predicted local viability calculated from the local UV-C dosage as a function of the relative position inside the four layers of the N95 mask illuminated from each side together with 1000 mJ/cm^2 surface dosage. Model 1 (*black*) uses the empirical double-exponential model to describe the UV-C dose-dependent inactivation shown in Fig. 3. Model 2 (*cyan*) uses a UV-C sensitivity of 0.522 cm^2/mJ, corresponding to the fast, initial virus inactivation process from Fig. 3. Model 3 (*red*) uses a UV-C sensitivity of 3.77 cm^2/mJ, which describes the UV-C inactivation of MHV coronavirus aerosols. (*B*) Predicted total virus viability from integration of the local viability over all mask layers as a function of total surface dosage equally divided across both sides for the three models. To see this figure in color, go online.

Based on the data from Fig. 3 *E*, model 1 predicts virus inactivation as a function of UV-C exposure, accounting for the possibility of virus populations with different UV-C sensitivities (22,24). The predicted local viability (*black curves* in Figs. 5 *B* and 6 *A*) shows the difficulty of inactivating the virus in the core of the shell and, to a smaller extent, in filter 2, but the model demonstrates sufficient decontamination to prevent surface transmission for reuse of an N95 mask, despite the 1.4% of the virus population that shows reduced UV-C sensitivity. However, we suspect that the UV-C sensitivity predicted by Kariwa et al. may be underestimated because of confounding inner-filter effects in the experimental assay (see Potential confounds in measurement of viral UV-C sensitivity in the Discussion).

Therefore, we created model 2 (*cyan curves* in Fig. 6), which assumes that the major population, consisting of 98.6% of virus, has a UV-C sensitivity of 0.522 cm^2/mJ based on observations from Kariwa et al. (22,24). The local virus viability in the shell is similar in both models 1 and 2. However, because of the lack of the UV-C resistant minor population in model 2, more virus is inactivated in filter 2 because the UV-C resistant minor population is the main contributor at low percentage values of local viability. Model 3 (*red curves* in Fig. 5) is similar to model 2 but assumes a higher UV-C sensitivity of 3.77 cm^2/mJ based on the measured UV-C sensitivity murine hepatitis virus (MHV) coronavirus in aerosol (30). Model 3 suggests complete inactivation of virus in all layers of the mask, including the highly shielded core of the shell.

We calculated the total virus viability averaged over all layers, as obtained from the integrated local viabilities, for the three different models as a function of surface UV-C dosage (Fig. 6 *B*). The curves for model 1 (*black*) and model 2 (*cyan*) are similar for UV-C dosages up to 1000 mJ/cm^2 before they diverge. The surface dosages from each side necessary to achieve 2-log-order reduction to 1% total viability are 637 mJ/cm^2 for model 1 and 575 mJ/cm^2 for model 2. For 3-log-order reduction to 0.1% total viability, the dosage for model 1 with 1765 mJ/cm^2 is already noticeably larger than the 1068 mJ/cm^2 for model 2. Model 1 fails to achieve 4-log-order reduction for dosages up to 5000 mJ/cm^2, at which the total virus viability reduced to 0.011%. Model 2, on the other hand, reaches 4-log-order reduction to 0.01% at 1597 mJ/cm^2, 5-log-order reduction at 2145 mJ/cm^2, and 6-log-order reduction at 2705 mJ/cm^2. In comparison, the high UV-C sensitivity in model 3 predicts 3-log-order reduction at 148 mJ/cm^2 and 6-log-order reduction at 375 mJ/cm^2. Model 3 shows robust UV-C sensitivity and corresponds to a 3-log reduction with notably lower UV dosage compared with model 1 and model 2.

DISCUSSION

In this section, we review literature and outline principles and points of consideration when implementing UVGI decontamination of N95 masks. The optimization of the UV-C dosage for efficient decontamination of a mask depends on several design parameters. What degree of reduction of virus viability is desired? Is it necessary to decontaminate interior layers of the mask that are inaccessible for direct contact? Does the applied UV-C dosage negatively affect the performance of the mask? Is it practical to deliver the necessary dosage?

N95 mask filtration efficiency for aerosolized viruses

Aerosolized MS2 virions permeate N95 masks with a peak permeability exceeding 5% for particles with ~50-nm diameter (31,32), but the permeability is below 1% for aerosolized MS2 at 500-nm average particle diameter (33). Studies have demonstrated that N95 masks trap MS2 virions in small aerosol particles (with 141 nm median diameter) preferentially in the middle layer, whereas virions in larger aerosol particles (median diameter 492 nm) are preferentially trapped in the outer layer (34). The only study that

used aerosolized adenovirus and influenza virus found levels of permeability comparable with the results from the MS2 model virus, even though the MS2 virion (27.5-nm diameter) is smaller than influenza virus (80- to 120-nm diameter) or SARS-CoV-2 (50- to 200-nm diameter) (35). This suggests that the size of the aerosol particles carrying virions, not the size of the virions themselves, is the important factor for the efficacy of the N95 mask's mechanism of action.

Hospital samples of SARS-CoV-2 aerosols collected during the outbreak in Wuhan, China showed viral RNA present in a distribution of differently sized aerosols with multiple peaks: one in submicron region (particle diameter of 250 nm to 1 μm) and another in the supermicron region (particle diameter larger than 2.5 μm), but also in even smaller particles (range 10–250 nm) (36). It is noteworthy that live virions in environmental aerosols are key to transmission, and it is difficult to quantify compared to viral RNA alone. Quantification from Liu et al. is based on quantitative reverse transcriptase polymerase chain reaction (RT-qPCR) assays of viral RNA instead of culturing viable virions (37). Based on studies using a similar distribution of differently sized MS2 aerosol particles, a large fraction of the supermicron and submicron SARS-CoV-2 particles would be trapped in the outer layer of N95 masks, whereas the smaller particles should get trapped in the microfiber material of the middle layer.

Routes of transmission via N95 mask extended use and reuse

For decontamination of N95 masks, it is important to consider which parts of the multilayer structure provide potential viral transmission risk. Risk of contact transmission is due to handling the contaminated surface of a mask (8). It is also possible that virus could be reaerosolized from the mask because of the airflow from breathing, coughing, or sneezing. A study of simulated coughing through an N95 mask contaminated with the MS2 virus demonstrated that only a small percentage of virus was released (38). However, SARS-CoV-2 RNA was present at high levels in large-particle aerosols in hospitals during the COVID-19 outbreak, which raises concerns that larger particles are more efficiently reaerosolized under similar conditions (36,39). Our results demonstrate that inner layers of the N95 mask will inevitably receive different amounts of dosage than outer layers. Decontamination methods must consider the efficacy of inactivating virions most importantly on the masks' surface, as well as on the inner layers of the mask.

Potential confounds in measurement of viral UV-C sensitivity

The prediction and measurement of the sensitivity of novel viruses to germicidal UV light is an important and difficult problem (20,23,40). Several studies have investigated UV-C sensitivity for coronaviruses, including SARS-CoV (22,24,28,41,42) and SARS-CoV-2 (43).

A confound in these studies is that the virus preparations are made in Dulbecco's modified Eagle's medium (DMEM) including 10% fetal bovine serum (FBS) and other additives, such as antibiotics and antifungals. The high protein content of FBS results in a high absorbance at 254 nm. We determined that 10% FBS contributes 1.54 $\pm$ 0.04 and DMEM contributes 1.12 $\pm$ 0.02 absorbance at 254 nm. The absorbance is $\sim$2.66 $\pm$ 0.04 per 1-cm pathlength with $\sim$58% contribution from FBS and the rest from DMEM. Therefore, even shallow layers of virus suspension will have a high absorbance that results in substantial inner-filter effects that reduce the available UV-C dosage in a depth-dependent fashion. (For clarity, we would like to note that the "inner-filter effect" is a principle in fluorescence spectroscopy and has no relation in concept to N95 mask filters.)

These inner-filter effects likely explain the discrepancies between two studies with SARS-CoV, in which the reduction of the filling height of the virus suspension from 1 to 0.25 cm resulted in 40-fold increase of UV-C sensitivity from 0.012 to 0.477 cm^2/mJ (22,28). The UV-C sensitivity of a different coronavirus, MHV, in aerosol form was 3.77 cm^2/mJ (30), which is even eightfold higher than SARS-CoV in the shallow solution. The RNA genome size of the different coronaviruses (MHV, SARS-CoV, and SARS-CoV-2) is very similar (44,45), and therefore, they should have intrinsically similar UV-C sensitivities (20,23,40). The differences of UV-C sensitivities are likely due to the different form: aerosol versus shallow solution. Because the small diameter of the aerosol droplets will have negligible inner-filter effects, UV-C sensitivities measured in aerosol are the most applicable, although to perform these experiments on additional viral species is prohibitive because of the requisite biosafety measures.

UV-C inactivation of the Berne virus or equine torovirus, closely related to coronaviruses and with a similar RNA genome size (46), has been measured in very shallow preparations of $\sim$0.05-cm pathlength (29). The corresponding UV-C sensitivity is 3.24 cm^2/mJ, which is very close to that for the MHV aerosols, additionally supporting that the high UV-C sensitivity inferred from the aerosols and is most closely reflected by values determined by solutions with minimal inner filter artifacts. Future studies of the UV-C sensitivity of SARS-CoV-2 should carefully address the issue of UV attenuation due to the sample media composition, for example, by using very thin solution layers or by using virus purified in low UV-absorbing buffers.

Potential methods for validating N95 decontamination

In addition to developing models that predict UV-C penetration into masks and inactivation of SARS-CoV-2, the

reduction in viral bioburden in N95 masks could potentially be measured directly. Oral et al. demonstrated the effectiveness of vaporized hydrogen peroxide decontamination by applying SARS-CoV-2 to the surface of an N95 mask and assessing the effect of treatment through quantifying extracted of viable virus from mask sections (47). Future work could employ this technique to assess the ability of UV-C to affect viability of SARS-CoV-2. However, this method of measuring bioburden reduction has a key limitation; the static application of the virus to the respirator surface does not accurately model the penetration of aerosolized virus deeper into the respirator. Although virus on the surface likely poses the greatest hazard to the user and others, one study using the MS2 bacteriophage as a model has shown that a small percentage of viable virus can be reaerosolized from an N95 respirator (27). Aerosolization of the virus before exposure is prohibitively dangerous, requiring a biosafety level 4 laboratory.

Small-scale implementation of UVGI for N95 masks

Many groups have focused on large-scale chambers to accommodate up to 27 masks in one cycle with two planar 12 UV-C bulb arrays (48,49). However, biosafety cabinets and even medium-scale UVGI boxes that hold six masks demonstrate variability in UV dosage as a result of distance, angle of incidence from light source, and orientation and shape of the masks (50,51). The higher UV-C doses needed to compensate for this variability and ensure decontamination may increase the risk of compromising masks' structural integrity. By contrast, a single-mask decontamination system can ensure that a controlled, carefully measured UV-C dose is delivered to the mask. In addition, such a system would be cheap and practical for point-of-care decontamination outside of hospital settings.

We used a commercial UVP cross-linker that has 5× 8-W 254-nm mercury-vapor bulbs in an enclosure. A microprocessor controls the UV-C exposure and stops the irradiation when the desired energy is delivered. Because the bulbs are only at the top of the enclosure, we needed to use two sequential exposures, flipping the mask upside down between them. The need to flip the masks adds another handling step with the risk of viral contamination. Point-of-use UV-C decontamination of N95 masks could prove useful to frontline workers, such as firefighters, transit workers, and grocery store employees, who would need to decontaminate small numbers of respirators and would lack access to the bulk respirator decontamination systems now being implemented in hospitals.

Photodegradation of the masks

One concern with UV-C decontamination of N95 respirators is that photodegradation could limit the number of times that a mask can be reused safely. The photodegradation of polypropylene filaments by UV-C irradiation has been studied with mechanical strength tests and Fourier transform infrared spectroscopy, which has demonstrated the formation of alcohols, peroxides, ketones, aldehydes, carboxylic acids, and anhydride reaction products (52,53). The initiation of photo-oxidation reaction cascades of polypropylene, especially at wavelengths longer than 290 nm, is thought to originate from chromophoric groups such as hydroperoxides, which in turn are formed in an autocatalytic process (54). The photodegradation of the polyester poly(ethylene terephthalate) involves photo-oxidative reactions leading to chain scission and the generation of carboxyl end groups (55,56). The photodegradation of polypropylene and polyester both rely on photo-oxidative reactions involving reactive oxygen species (ROS).

Several studies have previously examined the effect of UV-C irradiation on N95 respirator filtration and fit. However, their findings vary widely. According to Lindsley et al., for four tested N95 models, the mechanical strength of one or more layers was significantly reduced at exposure doses higher than 120,000 mJ/cm^2 sequentially applied to each side (57). The researchers observed only minor changes in particle penetration and flow resistance as a result, suggesting that a mask could safely endure 120 decontamination cycles of 1000 mJ/cm^2 (the Centers for Disease Control and Prevention-recommended standard). However, this study only looked at filtration efficiency rather than quantitative fit factor, which is inversely proportional to the total inward leakage of particles through a worn respirator. Fit factor, therefore, measures overall respirator performance, including both filtration efficiency and fit to the user's face. Smith et al. found that the fit factor of masks was reduced (albeit not below the minimal standard for N95s) after a dose of 18,000 mJ/cm^2 via a germicidal lamp in a biosafety cabinet, corresponding to only 18 such cycles (58). We note that Smith et al. used different models of N95 masks (1860, Aura 1870+, industrial 8511) manufactured by 3M, although no data were provided investigating differential effects of UV-C for each model. Another study of the effect of UV-C irradiation on the fit test performance of N95 masks did not have data for the 3M 8210 mask because of the current supply shortage (59). They found that fit factor began to decrease even before 10 decontamination cycles, but the UV-C dose received by the mask was not specified, similar to a report by Fischer et al. (22).

We conducted our own tests, exposing two 3M model 8210 N95 respirators to repeated doses of UV-C (with either 5000 or 10,000 mJ/cm^2 exposure doses per side). Before and after each cycle, the masks were donned by a volunteer, and the quantitative fit factor was measured using a TSI PortaCount Pro Plus (Shoreview, MN). The quantitative fit factor is defined as the ratio of concentrations of

0.02–1 μm particles outside and inside the mask and is decreased both by particle penetration and poor fit. For N95 masks and other disposable respirators, the PortaCount Pro can measure a maximal fit factor of 200 (which would correspond to the mask filtering at least 99.5% of particles). One mask was subjected to 14 exposure cycles (5000 mJ/cm^2 per cycle per side) and the other to one long exposure (20,000 mJ/cm^2 exposure doses per side) followed by six shorter cycles (10,000 mJ/cm^2 per side), giving 80,000 mJ/cm^2 total dosage per side. Both tested masks maintained a fit factor of 200 during both normal breathing and deep breathing throughout for exposures up to 50,000 mJ/cm^2 total dosage per side, which would correspond to 50 decontamination cycles with 1000 mJ/cm^2 each per side. We caution that this result is likely dependent on the model of N95 used, which may contribute to the inconsistency of results obtained from the literature. The company 3M has recently posted a technical bulletin on the impact of decontamination methods on selected N95 mask models from their program, including the 3M 8210 model we used in our experiments. They evaluated five UV-C decontamination systems and found that all of them pass the filtration efficiency and fit tests for five or more reprocessing cycles with exposure dosages of $\geq$1000 mJ/cm^2 on each side, and in one case up to a cumulative lifetime exposure of 100,000 mJ/cm^2 (60). Further testing is needed on other N95 models to determine the number of decontamination cycles that they can withstand without compromise.

We did observe that the UV-C irradiation of our N95 masks resulted in a slight odor of the masks that appeared to originate from the polyester material of the shell layer, as the odor was similar upon irradiation from both sides or only the inside, where all the light is absorbed by the shell layer. The odor originates from the UV-C irradiated mask itself and not any residues from wearing the mask because a never-worn, new mask gives the same result. The odor is weak and dissipates rapidly but nevertheless might reduce the acceptance of UV-C decontamination of N95 masks for sensitive individuals. We also irradiated a N95 mask in a nitrogen atmosphere to test the role of ROS in the odor formation during photodegradation of the N95 mask. As compared with a mask irradiated in air, the nitrogen atmosphere dramatically reduced the subjective odor formation. Although the ROS exposure might aid with virus inactivation, the UVC radiation alone should be sufficient for mask decontamination. Nitrogen can easily be purified from air by filtration, and it could be used for UV-C decontamination equipment to reduce odor formation and thereby improve the user acceptance of the decontaminated masks. Others have described a nutty or smoky odor of masks after UV-C decontamination and recommended allowing for off-gassing time when feasible (48). Odor has been reported for moist heat decontamination methods as well (61).

Present and future importance of N95 emergency reuse

Epidemiological reports indicate that the number of infectious disease outbreaks tripled between 1980 and 2010 (62), indicating a high likelihood of future moments of acute need for PPE such as N95 masks. It is difficult to prepare or stockpile N95 masks supplies in anticipation of this, given that current models of N95s can have a shelf life of 5 years and decrease in effectiveness after their manufacturer-designated expiration date (7,8). Furthermore, challenges in increasing N95 production may not allow demand to be reached quickly enough during critical early moments of the spread of a disease and suggests that emergency N95 reuse is a necessary option to maintain. We note that 2 months after initial shortages of N95s due to COVID-19, demand has still not been met for health care workers treating infected individuals (63). Therefore, we suggest that decontamination methods, such as UVGI of N95 masks, be considered as a feature of preparedness for times of acute need of PPE.

The experiments that went into this study were performed during the extraordinary circumstances of working from March to May in the epicenter of the spring peak of the COVID-19 pandemic in New York City. Our study provided the foundation for the Rockefeller University N95 mask reuse with decontamination program, in which we used Stratalinker UV-C sources and later in-house engineered UV-C irradiators. The program allowed the university to conserve N95 mask supplies and enabled critical university personnel to safely use mass transportation. The results of our study were disclosed as a preprint (64) in the beginning of June 2020. Preprints are snapshots in time of science that sometimes is in rapid flux. Since then, related results were published in several preprints and published works discussed below (36,65–80).

Storm et al. measured viral viability over time as wet and dry droplets of SARS-CoV-2, both exposed and unexposed to UV-C radiation (77). The authors report a decay time constant for single exponential decay function fit of the normalized viral viability of wet virus over time. From the reported inactivation time constant of 1.0 $\pm$ 0.1 s and the UV-C power density of 0.849 mW/cm^2, we calculated a UV-C sensitivity of 1.18 $\pm$ 0.12 cm^2/mJ). However, we found by inspection and refitting of their tabulated data that about half of the virus must have been inactivated within the deadtime of their experiment, which suggests the presence of a second component with higher UV-C sensitivity. Moreover, the limited amounts of infectious particles used for each experiment do not allow the detection of more highly UV-C resistant fractions. Overall, the data from the Storm et al. study (77) present an advance because the authors were able to obtain results for SARS-CoV-2 in a biosafety level 4 laboratory, and they avoided the abovementioned issues with inner filter effects of the protein-rich tissue culture

media by using very small droplet volumes (5 μL). We calculate the UV-C dosage of 5.9 or 11.7 mJ/cm^2 needed to achieve 3-log or 6-log order, respectively, of virus inactivation from this new value for the UV-C sensitivity of SARS-CoV-2. Bianco et al. reported in a preprint that UV-C dosage of 3.7 mJ/cm^2 was sufficient to achieve a 3-log-order inactivation of SARS-CoV-2 suspended in tissue culture media in a 1-mm-thick layer (65), but their data lack the information at low UV-C dosages necessary to calculate the UV-C sensitivity.

Two studies addressed the light propagation inside a N95 mask. Sears et al. modeled the effects of uneven UV-C exposure of masks from two sides due to mask curvature, and they suggest the use of multidirectional UV-C irradiation to improve decontamination (76). Lilge et al. determined the optical scattering and absorbance coefficients of several N95 mask materials using diffuse transmission and reflection measurements with an integrating sphere and an array spectrophotometer, and they used these parameters for Monte Carlo modeling the light distribution within the layers of the mask (70). Their modeling of the single-sided light distribution within the 3M 8210 mask suggests about 4-log-order reduction from the surface light fluence. The integrating sphere data now allow us to extend our own modeling to include the effects of UV-C reflectivity between layers of the N95 mask. Fig. 7 shows the results of the model described in the Appendix. The model suggests that with an exposure dosage with 1000 mJ/cm^2 from both sides of the mask, the minimal internal local dosage will be 28 mJ/cm^2, which is sufficient to yield better than log-6 inactivation of SARS-CoV-2 based on the data from Storm et al. (77). Notably, this minimal local dosage calculated from the model including reflections is fourfold higher as compared with the model presented in Fig. 5, despite using the same experimental values of the transparency for each layer.

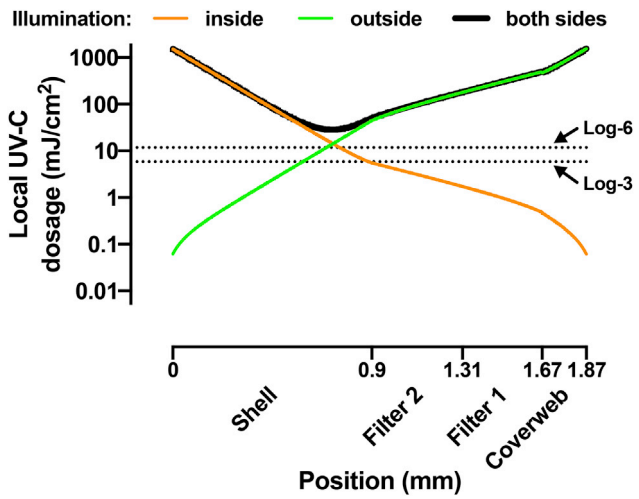

FIGURE 7 Modeling of the UV-C dosage in different layers of the N95 mask including the effects of reflectivity. Local UV-C dosage is shown as a function of the position inside the four layers of the N95 mask. The three different curves show the local UV dosage for three cases of illumination: illumination from the inside only (*orange*), illumination from the outside only (*green*), and illumination from both sides (*black*) with 1000 mJ/cm^2 surface UV-C dosage. The dotted lines indicate the UV-C dosage necessary to achieve log-3 and log-6 level inactivation of SARS-CoV-2 using recently published data (77). To see this figure in color, go online.

Other studies addressed the rate of viral inactivation within an N95 mask. Kayani et al. (69) measured inactivation over time for several pathogens, including the MS2 virus, on the surface of two N95 masks, including the 3M 1860. They found that a dose of $\sim$2 J/cm^2 yielded a >4-log-order reduction in MS2 surface bioburden (69). Golovkine et al. (68) performed a similar study using SARS-CoV-2 and for the 3M 1860 respirator obtained similar results; a dose ranging from 900 to 1620 mJ/cm^2 on different areas of the mask achieved a 3.7-log-order reduction of virus on the mask surface. However, they found that the same dose achieved only a 1.7-log-order reduction on a 3M 8210 mask (68). Ozog et al. performed a similar study on five different N95 respirators, including both the 3M 1860 and 3M 8210; similarly, they found that a 1.5 J/cm^2 of exposure per side reduced SARS-CoV-2 bioburden on the 3M 1860 facepiece below the limit of detection but failed to do so on the 3M 8210 facepiece (81). They suggest that mask materials with hydrophilic properties, such as the 3M 8210, may have absorbed the virus applied to the surface deeper within the mask, and therefore, the mask shielded some virus from UV-C radiation.

Rathnasinghe et al. (73) examined total viral viability throughout the mask; they incubated squares of N95 mask material (3M 8211) in media spiked with SARS-CoV-2 before exposing them to varying doses of UV-C. Viral viability was measured after decontamination and fitted as a function of UV-C dose to a single exponential curve (73). However, inspection of their data reveals that the time resolution of their experiment is insufficient to resolve the UV-C dose-dependent inactivation kinetics. Moreover, the 3M 8211 N95 mask they used has a release valve, which is generally considered an exclusion criterion for use of UV-C decontamination. Using a similar method, Ludwig-Begall et al. found that doses of 2.6 and 5.2 J/cm^2, applied to a surgical mask and a KN95 respirator, respectively, yielded a >3-log-order reduction in viable porcine respiratory coronavirus (71). This result suggests that UVGI is broadly effective to decontaminate disposable masks and respirators, but further work is needed to ensure that filtration is unaffected and to determine whether the standard dose of 1 J/cm^2 is sufficient for decontamination.

On the regulatory side, a nonbinding recommendation issued by the Food and Drug Administration (FDA) contained three tiers for N95 respirator decontamination (82). The highest level is recommended for decontamination of surgical masks for single or multiple users and includes a 6-log reduction of highly resistant bacterial spores. The second

tier is intended for single users only and specifies a 6-log-order reduction of nonenveloped viruses or vegetative bacteria. The third tier recommends 3-log-order reduction of nonenveloped virus or vegetative bacteria, and it is intended for single users only to supplement existing Centers for Disease Control and Prevention reuse recommendations. One of the key problems with these guidelines is that they do not specify how the bioburden reduction should be measured, in particular, where in the mask should the test be performed. Is it sufficient to obtain the desired reduction for a test sample applied to the surface of the mask, or is the same degree of reduction required for a sampled applied to any of the internal layers of the multilayer structure of the N95 mask? We noted that the user-facing shell layer of the 3M 8210 mask is the most problematic because of its high degree of UV-C absorption. In a single-user setting, the main aim is to decontaminate any virus that became trapped in the middle layers of the mask during use.

CONCLUSION

Several strategies have been used to decontaminate N95 masks during the COVID-19 pandemic, most of which are being developed for large-scale applications. Here, we review the efficacy of UV-C decontamination for N95s, considering factors such as UV transmittance to different layers of the mask, viral sensitivity to UV-C, and potential photodegradation of masks. We also describe the use of a UV cross-linker box commonly found in molecular biology laboratories as a practical, point-of-use method for small-scale rapid UV-C decontamination of N95 masks. Such devices assure that a consistent dose of UV-C is applied to the masks, enabling reliable decontamination and repeated reuse without substantial mask photodegradation. Mass production of similar custom low-cost devices could be a cost-effective way of empowering frontline workers, and potentially the general public, to decontaminate masks even if they lack access to a large hospital-based decontamination facility.

APPENDIX: MODELING THE LIGHT DISTRIBUTION IN A MULTILAYER STRUCTURE ACCOUNTING FOR DIFFUSE REFLECTANCE

Our original model describes the depth-dependent transmittance and optical thickness as the integral of a depth-dependent attenuation coefficient (Eq. 3). We could not discriminate the relative contributions from absorbance and scattering to this attenuation coefficient because we did not have a setup to measure reflectivity. Lilge et al. studied the light distribution within N95 masks and provide data for the relative strength of absorbance and scattering coefficients of the materials in the 3M 8210 mask from integrating sphere reflectance and transmittance measurements (70). Here, we extend our model using the Kubelka theory (83,84) to include the contributions of diffuse reflectance on the light distribution within the multilayer structure of the N95 mask.

Table 1 shows the values of the absorption and scattering coefficients, μ_a and μ_s, for the different layers of the 3M 8210 mask. The authors used the terms outer layer for the coverweb, filter for the combined layers filter 1 and filter 2, and inner layer for the shell. However, they did not determine the thickness (d) for each mask layer and set it to some rather arbitrary values in their calculations of μ_a and μ_s. Therefore, these parameters have to be adjusted to be used with the layer thicknesses we measured for our masks.

TABLE 1 Optical properties of the materials in the 3M 8210 mask

	μ_a (mm^{-1})	μ_s (mm^{-1})	d (mm)	a	P	T	R_0
Outer layer	0.386	1.926	0.98	1.200	1.887	0.208	0.504
Filter	0.222	3.116	1.77	1.071	5.515	0.064	0.682
Inner layer	0.894	4.187	1.05	1.213	4.396	0.035	0.525
Coverweb	1.813	9.044	0.2	1.200	1.809	0.22	0.501
Filter 1	0.510	7.154	0.36	1.071	2.575	0.21	0.633
Filter 2	0.615	8.628	0.41	1.071	3.538	0.14	0.662
Shell	2.016	9.444	0.9	1.213	8.499	0.0021	0.526
Filter 1 + 2	–	–	–	–	–	0.051	0.684

We calculate the dimensionless ratio

$$a = (\mu_a + \mu_s)/\mu_s \tag{14}$$

from the Lilge et al. data (70) and numerically solve the transmittance equation

$$T = \frac{b}{a \sinh bP + b \cosh bP} \tag{15}$$

with

$$b = \left(a^2 - 1\right)^{\frac{1}{2}} \tag{16}$$

for the scattering power, P, using our experimental values for the transmittance T.

The scattering power scales with the layer thickness d in the case of a homogeneous layer with the scattering coefficient μ_s:

$$P = \mu_s d. \tag{17}$$

We obtain the scattering coefficient by inverting Eq. 17:

$$\mu_s = P/d. \tag{18}$$

The absorption coefficient can now be calculated as

$$\mu_a = (a - 1)\mu_s. \tag{19}$$

The reflectance, R, of a layer with nonreflecting backing is calculated as

$$R = \frac{\sinh bP}{a \sinh bP + b \cosh bP}. \tag{20}$$

The combination of two layers, 1 and 2, results in a combined transmittance, $T_{1,2}$, and reflectance, $R_{1,2}$, given by (84)

$$T_{1,2} = \frac{T_1 T_2}{1 - R_I R_2} \tag{21}$$

and

$$R_{1,2} = R_1 + \frac{T_1^2 R_2}{1 - R_I R_2}, \tag{22}$$

with the transmittances T_1 and T_2 and the reflectances R_1 and R_2 of both layers measured in one direction following the order of the layers 1 and 2. The expressions also use the reflectance of layer 1 in reverse direction as indicated with the roman numeral index, R_I. Note that the reflectances from the front (R_1) and back (R_I) of a homogeneous layer are identical, but they are not identical for stacks of different materials. We use Eqs. 21 and 22 to calculate the transmittance and reflectance of the combined filter 1 and filter 2 (see Table 1) for comparison with the data for the filter layer from Lilge et al. (70).

We are interested in the total amount of light present in the interior of the mask. At the interface of two layers, 1 and 2, the fraction T_1 of light transmitted through layer 1 hits the layer 2, which reflects the portion T_1R_2. The portion T_1R_2 hits the back of layer 1, which reflects the portion $T_1R_2R_I$ and so on. The total fraction of the light at the interface of layers 1 and 2 can be obtained from

$$\begin{aligned} Total_{1,2} &= T_1 + T_1R_2 + T_1R_2R_I + T_1R_2^2R_I + T_1R_2^2R_I^2 + \ldots \\ &= T_1\frac{1+R_2}{1-R_IR_2}. \end{aligned} \tag{23}$$

The generalization of Eqs. 21, 22, and 23 from two layers to n layers is given by

$$T_{1,2,3,\ldots n} = \frac{T_1T_{2,3,\ldots n}}{1-R_IR_{2,3,\ldots n}}, \tag{24}$$

$$R_{1,2,3,\ldots n} = R_1 + \frac{T_1^2R_{2,3,\ldots n}}{1-R_IR_{2,3,\ldots n}}, \tag{25}$$

and

$$Total_{i,j} = T_{1,2,\ldots i}\frac{1+R_{j,j+1,\ldots n}}{1-R_{i,i-1,\ldots 1}R_{j,j+1,\ldots n}}. \tag{26}$$

To calculate the light distribution within one layer, we split it in two parts, a and b, with thicknesses $d_a = \lambda d$ and $d_b = (1-\lambda)d$ and calculate the transmittance and reflectance of the sublayers using Eqs. 15, 17, and 20:

$$T_a = \frac{b}{a\sinh b\lambda P + b\cosh b\lambda P}, \tag{27}$$

$$R_a = \frac{\sinh b\lambda P}{a\sinh b\lambda P + b\cosh b\lambda P}, \tag{28}$$

$$T_b = \frac{b}{a\sinh b(1-\lambda)P + b\cosh b(1-\lambda)P}, \tag{29}$$

and

$$R_b = \frac{\sinh b(1-\lambda)P}{a\sinh b(1-\lambda)P + b\cosh b(1-\lambda)P}. \tag{30}$$

The four layers of the N95 mask (1, coverweb; 2, filter 1; 3, filter 2; and 4, shell) are separately split into sublayers to result in four different λ-dependent five-layer assemblies:

Stack 1: 1a, 1b, 2, 3, 4,
Stack 2: 1, 2a, 2b, 3, 4,
Stack 3: 1, 2, 3a, 3b, 4, and
Stack 4: 1, 2, 3, 4a, 4b.

The resulting layers can be used for Eqs. 24 to 25 to calculate the transmittance $T_{1,2,3,\ldots,n}$, reflectance $R_{1,2,3,\ldots n}$, and any of the interlayer total light fractions $Total_{i,j}$ for the multilayer system. Inversion of the order of layers yields the relevant equations for the illumination from the other side of the stack, $T_{n,n-1,\ldots,1}$, $R_{n,n-1,\ldots,1}$, and $Total_{j,i}$. The position d within the multilayer structure can be calculated as $d = \lambda d_1$, $d_1 + \lambda d_2$, $d_1 + d_2 + \lambda d_3$, or $d_1 + d_2 + d_3 + \lambda d_4$, respectively.

The local UV-C dosage, $D(d)$, between layers i and j can be calculated analogous to Eq. 9 from the surface exposure in the forward direction (D), the surface exposure in the reverse direction (D_R), and the depth-dependent transmittances:

$$D(d) = DTotal_{i,j} + D_RTotal_{j,i}. \tag{31}$$

AUTHOR CONTRIBUTIONS

T.H. and T.P.S. conceived and designed the experiments, collected the data, and performed the analysis. T.H., O.G., A.E.E., G.S., and T.P.S. reviewed the literature and wrote the manuscript.

ACKNOWLEDGMENTS

We thank the Rockefeller University laboratories of Drs. Paul Bieniasz, Frederick R. Cross, Seth A. Darst, Titia de Lange, Elaine Fuchs, Hironori Funabiki, Howard C. Hang, Mary E. Hatten, Sebastian Klinge, Roderick MacKinnon, Paul Nurse, Michael O'Donnell, Charles M. Rice, Michael P. Rout, Agata Smogorzewska, Hermann Steller, and Leslie B. Vosshall for generously providing access to their UV cross-linkers for this project. We thank Gaitree McNab, Frank X. Schaefer, and Amy Wilkerson of the Rockefeller University Department of Laboratory Safety and Environmental Health, and in particular Vichelle Filoteo, Eunice Jung, and Sachin Kadam for N95 fit testing. We also thank Bryan Baker, Ann H. Campbell, Dr. Daniel Gareau, Dr. Hiroyuki Takai, and Dr. Iltefat Hamzavi.

REFERENCES

1. Ranney, M. L., V. Griffeth, and A. K. Jha. 2020. Critical supply shortages - the need for ventilators and personal protective equipment during the covid-19 pandemic. *N. Engl. J. Med.* 382:e41.
2. WHO. 2020. Modes of transmission of virus causing COVID-19: implications for IPC precaution recommendations https://www.who.int/news-room/commentaries/detail/modes-of-transmission-of-virus-causing-covid-19-implications-for-ipc-precaution-recommendations.
3. Liao, L., W. Xiao, …, Y. Cui. 2020. Can N95 respirators be reused after disinfection? How many times? *ACS Nano.* 14:6348–6356.
4. FDA. 2007. Filtering facepiece respirator for use by the general public in public health medical emergencies - Class II special controls guidance for industry and FDA staff https://www.fda.gov/medical-devices/guidance-documents-medical-devices-and-radiation-emitting-products/filtering-facepiece-respirator-use-general-public-public-health-medical-emergencies-class-ii-special.
5. Carias, C., G. Rainisch, …, L. M. Koonin. 2015. Potential demand for respirators and surgical masks during a hypothetical influenza pandemic in the United States. *Clin. Infect. Dis.* 60 (*Suppl 1*):S42–S51.
6. FDA. 2020. Enforcement policy for face masks and respirators during the coronavirus disease (COVID-19) public health emergency (revised): guidance for industry and food and drug administration staff https://www.fda.gov/media/136449/download.

7. CDC. 2020. Decontamination and reuse of filtering facepiece respirators using contingency and crisis capacity strategies https://www.cdc.gov/coronavirus/2019-ncov/hcp/ppe-strategy/decontamination-reuse-respirators.html.
8. CDC. 2020. Recommended guidance for extended use and limited reuse of N95 filtering facepiece respirators in healthcare settings https://www.cdc.gov/niosh/topics/hcwcontrols/recommendedguidanceextuse.html.
9. Kobayashi, L. M., B. R. Marins, …, R. Castro. 2020. Extended use or reuse of N95 respirators during COVID-19 pandemic: an overview of national regulatory authority recommendations. *Infect. Control Hosp. Epidemiol.* 41:1364–1366.
10. Fisher, E., J. Williams, and R. Shaffer. 2010. The effect of soil accumulation on multiple decontamination processing of N95 filtering facepiece respirator coupons using physical methods. *J. Int. Soc. Respir. Prot.* 27:16–26.
11. Barrett, L. W., and A. D. Rousseau. 1998. Aerosol loading performance of electret filter media. *Am. Ind. Hyg. Assoc. J.* 59:532–539.
12. Heimbuch, B. K., W. H. Wallace, …, J. D. Wander. 2011. A pandemic influenza preparedness study: use of energetic methods to decontaminate filtering facepiece respirators contaminated with H1N1 aerosols and droplets. *Am. J. Infect. Control.* 39:e1–e9.
13. Mills, D., D. A. Harnish, …, B. K. Heimbuch. 2018. Ultraviolet germicidal irradiation of influenza-contaminated N95 filtering facepiece respirators. *Am. J. Infect. Control.* 46:e49–e55.
14. Heimbuch, B. K., and D. Harnish. 2021. ARA research to mitigate a shortage of respiratory protection devices during public health emergencies. Contract No. HHSF223201400158C, Applied Research Associates https://www.ara.com/news/ara-research-mitigate-shortage-respiratory-protection-devices-during-public-health-emergencies/.
15. Lowe, J. J., K. D. Paladino, …, M. E. Rupp. 2020. N95 Filtering facepiece respirator ultraviolet germicidal irradiation (UVGI) process for decontamination and reuse (Nebraska Medicine) https://www.nebraskamed.com/sites/default/files/documents/covid-19/n-95-decon-process.pdf.
16. Grossman, J., A. Pierce, …, S. R. Eckhouse. 2020. Institution of a novel process for N95 respirator disinfection with vaporized hydrogen peroxide in the setting of the COVID-19 pandemic at a large academic medical center. *J. Am. Coll. Surg.* 231:275–280.
17. Anderegg, L., C. Meisenhelder, …, J. M. Doyle. 2020. A scalable method of applying heat and humidity for decontamination of N95 respirators during the COVID-19 crisis. *PLoS One.* 15:e0234851.
18. Amesz, J., L. N. Duysens, and D. C. Brandt. 1961. Methods for measuring and correcting the absorption spectrum of scattering suspensions. *J. Theor. Biol.* 1:59–74.
19. Beck, S. E., R. A. Rodriguez, …, K. G. Linden. 2015. Comparison of UV-induced inactivation and RNA damage in MS2 phage across the germicidal UV spectrum. *Appl. Environ. Microbiol.* 82:1468–1474.
20. Kowalski, W. J., W. P. Bahnfleth, and M. T. Hernandez. 2009. A genomic model for predicting the ultraviolet susceptibility of viruses. *IUVA News.* 11:15–28.
21. McDevitt, J. J., K. M. Lai, …, D. K. Milton. 2007. Characterization of UVC light sensitivity of vaccinia virus. *Appl. Environ. Microbiol.* 73:5760–5766.
22. Kariwa, H., N. Fujii, and I. Takashima. 2004. Inactivation of SARS coronavirus by means of povidone-iodine, physical conditions, and chemical reagents. *Jpn. J. Vet. Res.* 52:105–112.
23. Lytle, C. D., and J. L. Sagripanti. 2005. Predicted inactivation of viruses of relevance to biodefense by solar radiation. *J. Virol.* 79:14244–14252.
24. Kariwa, H., N. Fujii, and I. Takashima. 2006. Inactivation of SARS coronavirus by means of povidone-iodine, physical conditions and chemical reagents. *Dermatology.* 212:119–123.
25. Atwood, K. C., and A. Norman. 1949. On the interpretation of multi-hit survival curves. *Proc. Natl. Acad. Sci. USA.* 35:696–709.
26. Chen, H., A. Baitenov, …, L. Berglund. 2019. Thickness dependence of optical transmittance of transparent wood: chemical modification effects. *ACS Appl. Mater. Interfaces.* 11:35451–35457.
27. Fisher, E. M., and R. E. Shaffer. 2011. A method to determine the available UV-C dose for the decontamination of filtering facepiece respirators. *J. Appl. Microbiol.* 110:287–295.
28. Darnell, M. E., K. Subbarao, …, D. R. Taylor. 2004. Inactivation of the coronavirus that induces severe acute respiratory syndrome, SARS-CoV. *J. Virol. Methods.* 121:85–91.
29. Weiss, M., and M. C. Horzinek. 1986. Resistance of Berne virus to physical and chemical treatment. *Vet. Microbiol.* 11:41–49.
30. Walker, C. M., and G. Ko. 2007. Effect of ultraviolet germicidal irradiation on viral aerosols. *Environ. Sci. Technol.* 41:5460–5465.
31. Balazy, A., M. Toivola, …, S. A. Grinshpun. 2006. Manikin-based performance evaluation of N95 filtering-facepiece respirators challenged with nanoparticles. *Ann. Occup. Hyg.* 50:259–269.
32. Eninger, R. M., T. Honda, …, S. A. Grinshpun. 2008. Filter performance of n99 and n95 facepiece respirators against viruses and ultrafine particles. *Ann. Occup. Hyg.* 52:385–396.
33. Gardner, P. D., J. P. Eshbaugh, …, K. C. Hofacre. 2013. Viable viral efficiency of N95 and P100 respirator filters at constant and cyclic flow. *J. Occup. Environ. Hyg.* 10:564–572.
34. Fisher, E., S. Rengasamy, …, R. Shaffer. 2009. Development of a test system to apply virus-containing particles to filtering facepiece respirators for the evaluation of decontamination procedures. *Appl. Environ. Microbiol.* 75:1500–1507.
35. Zuo, Z., T. H. Kuehn, and D. Y. Pui. 2013. Performance evaluation of filtering facepiece respirators using virus aerosols. *Am. J. Infect. Control.* 41:80–82.
36. Liu, Y., Z. Ning, …, K. Lan. 2020. Aerodynamic analysis of SARS-CoV-2 in two Wuhan hospitals. *Nature.* 582:557–560.
37. Tellier, R., Y. Li, …, J. W. Tang. 2019. Recognition of aerosol transmission of infectious agents: a commentary. *BMC Infect. Dis.* 19:101.
38. Fisher, E. M., A. W. Richardson, …, R. E. Shaffer. 2012. Reaerosolization of MS2 bacteriophage from an N95 filtering facepiece respirator by simulated coughing. *Ann. Occup. Hyg.* 56:315–325.
39. Qian, Y., K. Willeke, …, J. Donnelly. 1997. Performance of N95 respirators: reaerosolization of bacteria and solid particles. *Am. Ind. Hyg. Assoc. J.* 58:876–880.
40. Kowalski, W., W. Bahnfleth, and M. Hernandez. 2019. A genomic model for predicting the ultraviolet susceptibility of viruses and bacteria. *In* IUVA Conference Proceedings.
41. Duan, S. M., X. S. Zhao, …, X. P. Dong; SARS Research Team. 2003. Stability of SARS coronavirus in human specimens and environment and its sensitivity to heating and UV irradiation. *Biomed. Environ. Sci.* 16:246–255.
42. Liu, Y., Y. Cai, and X. Zhang. 2003. Induction of caspase-dependent apoptosis in cultured rat oligodendrocytes by murine coronavirus is mediated during cell entry and does not require virus replication. *J. Virol.* 77:11952–11963.
43. Fischer, R., D. H. Morris, …, B. Williamson. 2020. Assessment of N95 respirator decontamination and re-use for SARS-CoV-2. *medRxiv* https://doi.org/10.1101/2020.04.11.20062018.
44. Yount, B., M. R. Denison, …, R. S. Baric. 2002. Systematic assembly of a full-length infectious cDNA of mouse hepatitis virus strain A59. *J. Virol.* 76:11065–11078.
45. Wu, F., S. Zhao, …, Y. Z. Zhang. 2020. A new coronavirus associated with human respiratory disease in China. *Nature.* 579:265–269.
46. Stewart, H., K. Brown, …, A. E. Firth. 2018. Transcriptional and translational landscape of Equine torovirus. *J. Virol.* 92:e00589-18.
47. Oral, E., K. K. Wannomae, …, B. Emmal. 2020. Vapor H_2O_2 sterilization as a decontamination method for the reuse of N95 respirators in the COVID-19 emergency. *medRxiv* https://doi.org/10.1101/2020.04.11.20062026.

48. Schnell, E., M. J. Harriff, …, S. M. Smith. 2020. Homegrown ultraviolet germicidal irradiation for hospital-based N95 decontamination during the COVID-19 pandemic. *medRxiv* https://doi.org/10.1101/2020.04.29.20085456.

49. Hamzavi, I. H., A. B. Lyons, …, D. M. Ozog. 2020. Ultraviolet germicidal irradiation: possible method for respirator disinfection to facilitate reuse during the COVID-19 pandemic. *J. Am. Acad. Dermatol.* 82:1511–1512.

50. Card, K. J., D. Crozier, …, D. T. Weaver. 2020. UV sterilization of personal protective equipment with idle laboratory biosafety cabinets during the covid-19 pandemic. *medRxiv* https://doi.org/10.1101/2020.03.25.20043489.

51. Baluja, A., J. Arines, …, M. T. Flores-Arias. 2020. UV light dosage distribution over irregular respirator surfaces. Methods and implications for safety. *J. Occup. Environ. Hyg.* 17:390–397.

52. Aslanzadeh, S., and M. H. Kish. 2010. Photo-oxidation of polypropylene fibers exposed to short wavelength UV radiations. *Fibers Polym.* 11:710–718.

53. Mahmoodabadi, H. A., M. H. Kish, and S. Aslanzadeh. 2018. Photodegradation of partially oriented and drawn polypropylene filaments. *J. Appl. Polym. Sci.* 135:45716.

54. Feldman, D. 2002. Polymer weathering: photo-oxidation. *J. Polym. Environ.* 10:163–173.

55. Fechine, G. J. M., M. S. Rabello, …, L. H. Catalani. 2004. Surface characterization of photodegraded poly(ethylene terephthalate). The effect of ultraviolet absorbers. *Polymer (Guildf.).* 45:2303–2308.

56. Hurley, C. R., and G. J. Leggett. 2009. Quantitative investigation of the photodegradation of polyethylene terephthalate film by friction force microscopy, contact-angle goniometry, and X-ray photoelectron spectroscopy. *ACS Appl. Mater. Interfaces.* 1:1688–1697.

57. Lindsley, W. G., S. B. Martin, Jr., …, J. D. Noti. 2015. Effects of ultraviolet germicidal irradiation (UVGI) on N95 respirator filtration performance and structural integrity. *J. Occup. Environ. Hyg.* 12:509–517.

58. Smith, J. S., H. Hanseler, …, N. L. Stucky. 2020. Effect of various decontamination procedures on disposable N95 mask integrity and SARS-CoV-2 infectivity. *J. Clin. Transl. Sci* 1–5.

59. Price, A. D., Y. Cui, …, L. F. Chu. 2020. Is the fit of N95 facial masks effected by disinfection? A study of heat and UV disinfection methods using the OSHA protocol fit test. *medRxiv* https://doi.org/10.1101/2020.04.14.20062810.

60. 3M. 2020. Technical bulletin - Decontamination of 3M filtering facepiece respirators, such as N95 respirators, in the United States - Considerations https://multimedia.3m.com/mws/media/1851918O/decontamination-of-3m-filtering-facepiece-respirators-global-considerations.pdf&usg=AOvVaw1S-g6JzG1eL5wYzWsto_wm.

61. Viscusi, D. J., M. S. Bergman, …, R. E. Shaffer. 2011. Impact of three biological decontamination methods on filtering facepiece respirator fit, odor, comfort, and donning ease. *J. Occup. Environ. Hyg.* 8:426–436.

62. Smith, K. F., M. Goldberg, …, S. Ramachandran. 2014. Global rise in human infectious disease outbreaks. *J. R. Soc. Interface.* 11:20140950.

63. FDA. 2020. FAQs on shortages of surgical masks and gowns during the COVID-19 pandemic https://www.fda.gov/medical-devices/personal-protective-equipment-infection-control/faqs-shortages-surgical-masks-and-gowns-during-covid-19-pandemic.

64. Huber, T., O. Goldman, …, T. P. Sakmar. 2020. Principles and practice of SARS-CoV-2 decontamination of N95 masks with UV-C. *medRxiv* https://doi.org/10.1101/2020.06.08.20125062.

65. Bianco, A., M. Biasin, …, M. Clerici. 2020. UV-C irradiation is highly effective in inactivating and inhibiting SARS-CoV-2 replication. *medRxiv* https://doi.org/10.1101/2020.06.05.20123463.

66. De Santis, R., V. Luca, …, F. Lista. 2020. Rapid inactivation of SARS-CoV-2 with LED irradiation of visible spectrum wavelenghts. *medRxiv* https://doi.org/10.1101/2020.06.18.20134577.

67. Doughty, D. C., S. C. Hill, and D. W. Mackowski. 2021. Viruses such as SARS-CoV-2 can be partially shielded from UV radiation when in particles generated by sneezing or coughing: numerical simulations. *J. Quant. Spectrosc. Radiat. Transf.* 262:107489, Published online December 24, 2020.

68. Golovkine, G. R., A. W. Roberts, …, S. A. Stanley. 2020. Practical considerations for Ultraviolet-C radiation mediated decontamination of N95 respirator against SARS-CoV-2 virus. *medRxiv* https://doi.org/10.1101/2020.11.24.20237917.

69. Kayani, B. J., D. T. Weaver, …, I. Charnas. 2020. UV-C Tower for point-of-care decontamination of filtering facepiece respirators. *Am. J. Infect. Control* Published online November 10, 2020. https://doi.org/10.1016/j.ajic.2020.11.010.

70. Lilge, L., A. Manalac, …, R. Hofmann. 2020. Light propagation within N95 filtered face respirators: a simulation study for UVC decontamination. *J. Biophotonics.* 13:e202000232.

71. Ludwig-Begall, L. F., C. Wielick, …, E. Thiry. 2020. The use of germicidal ultraviolet light, vaporised hydrogen peroxide and dry heat to decontaminate face masks and filtering respirators contaminated with a SARS-CoV-2 surrogate virus. *medRxiv* https://doi.org/10.1101/2020.06.02.20119834.

72. Paul, D., A. Gupta, and A. K. Maurya. 2020. Exploring options for reprocessing of N95 Filtering Facepiece Respirators (N95-FFRs) amidst COVID-19 pandemic: a systematic review. *PLoS One.* 15:e0242474.

73. Rathnasinghe, R., R. F. Karlicek, …, P. Balchandani. 2020. Scalable, effective, and rapid decontamination of SARS-CoV-2 contaminated N95 respirators using germicidal ultra-violet C (UVC) irradiation device. *medRxiv* https://doi.org/10.1101/2020.10.05.20206953.

74. Rothe, M., E. Rohm, …, D. Lantagne. 2020. A systematic review of mask disinfection and reuse for SARS-CoV-2 (through July 10, 2020). *medRxiv* https://doi.org/10.1101/2020.11.11.20229880.

75. Sarkis-Onofre, R., R. do Carmo Borges, …, F. F. Demarco. 2020. Decontamination of N95 masks against coronavirus: a scoping review. *medRxiv* https://doi.org/10.1101/2020.07.11.20151399.

76. Sears, A. P., J. Ohayon, …, R. I. Pettigrew. 2020. Modeling-based UV-C decontamination of N95 masks optimized to avoid undertreatment. *medRxiv* https://doi.org/10.1101/2020.10.30.20223354.

77. Storm, N., L. G. A. McKay, …, A. Griffiths. 2020. Rapid and complete inactivation of SARS-CoV-2 by ultraviolet-C irradiation. *Sci. Rep.* 10:22421.

78. Su, A., S. M. Grist, …, A. E. Herr. 2021. Quantitative UV-C dose validation with photochromic indicators for informed N95 emergency decontamination. *PLoS One* **16**, e0243554.

79. Weaver, D. T., B. D. McElvany, …, J. G. Scott. 2020. UV decontamination of personal protective equipment with idle laboratory biosafety cabinets during the COVID-19 pandemic. *medRxiv* https://doi.org/10.1101/2020.03.25.20043489.

80. Wielick, C., L. F. Ludwig-Begall, …, E. Thiry. 2021. The use of germicidal ultraviolet light, vaporised hydrogen peroxide and dry heat to decontaminate face masks and filtering respirators contaminated with an infectious norovirus. *Infection Prevention in Practice.* 3:100111.

81. Ozog, D. M., J. Z. Sexton, …, Q. S. Mi. 2020. The effect of ultraviolet C radiation against different N95 respirators inoculated with SARS-CoV-2. *Int. J. Infect. Dis.* 100:224–229.

82. FDA. 2020. Recommendations for sponsors requesting EUAs for decontamination and bioburden reduction systems for surgical masks and respirators during the coronavirus disease 2019 (COVID- 19) public health emergency — Guidance for industry and food and drug administration staff https://www.fda.gov/regulatory-information/search-fda-guidance-documents/recommendations-sponsors-requesting-euas-decontamination-and-bioburden-reduction-systems-face-masks.

83. Kubelka, P. 1948. New contributions to the optics of intensely light-scattering materials. *J. Opt. Soc. Am.* 38:448–457.

84. Kubelka, P. 1954. New contributions to the optics of intensely light-scattering materials. 2. Nonhomogeneous layers. *J. Opt. Soc. Am.* 44:330–335.